

# Performance and optimization of X-ray grating interferometry

T. Thuerling and M. Stampanoni

*Phil. Trans. R. Soc. A* 2014 **372**, 20130027, published 27 January 2014

---

## References

[This article cites 23 articles](#)

<http://rsta.royalsocietypublishing.org/content/372/2010/20130027.full.html#ref-list-1>

## Subject collections

Articles on similar topics can be found in the following collections

[biomedical engineering](#) (143 articles)

[medical physics](#) (23 articles)

[optics](#) (44 articles)

## Email alerting service

Receive free email alerts when new articles cite this article - sign up in the box at the top right-hand corner of the article or click [here](#)

## Research



**Cite this article:** Thuring T, Stampanoni M.

2014 Performance and optimization of X-ray grating interferometry. *Phil. Trans. R. Soc. A* **372**: 20130027.

<http://dx.doi.org/10.1098/rsta.2013.0027>

One contribution of 16 to a Discussion Meeting Issue 'Taking X-ray phase-contrast imaging into mainstream applications' and its satellite workshop 'Real and reciprocal space X-ray imaging'.

### Subject Areas:

biomedical engineering, medical physics, optics

### Keywords:

X-ray grating interferometry, phase-contrast imaging, optimization, polychromatic performance

### Author for correspondence:

M. Stampanoni

e-mail: [marco.stampanoni@psi.ch](mailto:marco.stampanoni@psi.ch)

# Performance and optimization of X-ray grating interferometry

T. Thuring<sup>1,2</sup> and M. Stampanoni<sup>1,2</sup>

<sup>1</sup>Swiss Light Source, Paul Scherrer Institut, Villigen PSI, Switzerland

<sup>2</sup>Institute for Biomedical Engineering, Swiss Federal Institute of Technology, Zurich, Switzerland

The monochromatic and polychromatic performance of a grating interferometer is theoretically analysed. The smallest detectable refraction angle is used as a metric for the efficiency in acquiring a differential phase-contrast image. Analytical formulae for the visibility and the smallest detectable refraction angle are derived for Talbot-type and Talbot-Lau-type interferometers, respectively, providing a framework for the optimization of the geometry. The polychromatic performance of a grating interferometer is investigated analytically by calculating the energy-dependent interference fringe visibility, the spectral acceptance and the polychromatic interference fringe visibility. The optimization of grating interferometry is a crucial step for the design of application-specific systems with maximum performance.

## 1. Introduction

X-ray grating interferometry is a relatively new imaging technique, giving access to two physical contrast mechanisms in addition to the conventional absorption contrast. The phase shift or the scattering intensity of the X-ray beam are complementary effects to absorption, and thus can yield additional information through increased image contrast between two materials. Using a grating interferometer, the measurement of these signals is achieved by analysing a periodic interference pattern for any changes caused by a displacement (refraction, phase shift) [1,2] or an amplitude reduction (scattering) [3].

Grating interferometry for multi-modal imaging recently gained considerable attention because it does not necessarily rely on highly coherent radiation from synchrotron sources, but is compatible with low-brilliance X-ray tubes [4]. This triggered many studies, for instance in the bio-medical imaging field [5–7], showing the potential of this technique for mainstream applicability.

Although phase-shift interactions have a higher cross section than interactions by absorption for hard X-rays ( $\delta/\beta \approx 10^3$ ), the eventual gain in the contrast-to-noise ratio (CNR) of two materials strongly depends on the imaging technique itself. For grating interferometry, it has been demonstrated that this gain is mainly dependent on the beam coherence, but also on the spatial sampling (e.g. the pixel size) of the signals [8,9]. This impedes the applicability of this technique for imaging tasks where, for instance, lower spatial resolution (i.e. low-dose applications) is required, such as for medical computed tomography. On the other hand, the large set of parameters for a grating interferometer provides additional degrees of freedom for the system design and optimization. As opposed to a standard absorption-based imaging system, the performance is determined not only by the available source and detector systems, but also by the available grating technology.

The first step in the design of an imaging system is typically the selection of the design energy, which has to be compatible with the thickness and density of the objects to be examined. This determines the choice of an appropriate X-ray tube and detector system, enabling an efficient detection of X-rays in the desired energy range. Finally, an interferometer has to be designed that must be optimized for the given source and detector system.

Here, a mathematical framework for the optimization of the grating interferometer for a given source and detector system is presented. For the optimization, the concept of the smallest detectable refraction angle is used, which has also been referred to as the resolution of the refraction angle [10] or the sensitivity [11,12].

In §2, the smallest detectable refraction angle is derived from the signal-to-noise ratio (SNR) of a differential phase measurement. Owing to its dependence on visibility, the analytical formula for the visibility is used for a complete analytical description. In §3, the analytical optimization of the interferometer geometry, in particular the optimization of grating periods and duty cycles, is demonstrated. In §4, the polychromatic behaviour of a grating interferometer is studied by deriving the energy-dependent and the energy-integrated (polychromatic) interference fringe visibility. A detailed discussion about the difference of a  $\pi$  and a  $\pi/2$ -shifting phase grating for a polychromatic beam is presented. Apart from general and qualitative descriptions [13,14] or simulation case studies [15], the effect of a spectral bandwidth has so far mostly been neglected. However, understanding the dependency of the polychromatic performance of the grating interferometer is crucial for the efficient optimization of dedicated imaging systems based on conventional X-ray tubes.

The theoretical descriptions presented here of the performance by means of the smallest detectable refraction angle provide a comprehensive framework for the optimization of grating interferometry on imaging systems with a polychromatic beam.

## 2. System parameters and performance metrics

### (a) System parameters

Figure 1 shows a schematic of a typical grating interferometer and its geometric parameters. It can be distinguished between two types of interferometers, the Talbot-type interferometer [1,2], which uses two gratings (G1 and G2), and the Talbot-Lau-type interferometer [4], which uses an additional grating (G0). The beam splitter grating, or G1, is a phase grating which generates a periodic interference pattern of period  $p_2$  with maximum intensity oscillations at the distances  $d = d_m$ , which are given by [16]

$$d = d_m = \frac{l \cdot (m/\eta^2)d_T}{l - (m/\eta^2)d_T}. \quad (2.1)$$

The parameter  $m$  (odd integer) is the Talbot order,  $d_T = p_1^2/2\lambda$  is a fractional Talbot distance and  $\eta \in \{1, 2\}$  determines the introduced phase shift  $\phi$  of G1, which is given by  $\phi = \eta \cdot \pi/2$ . For  $\eta = 1$ ,

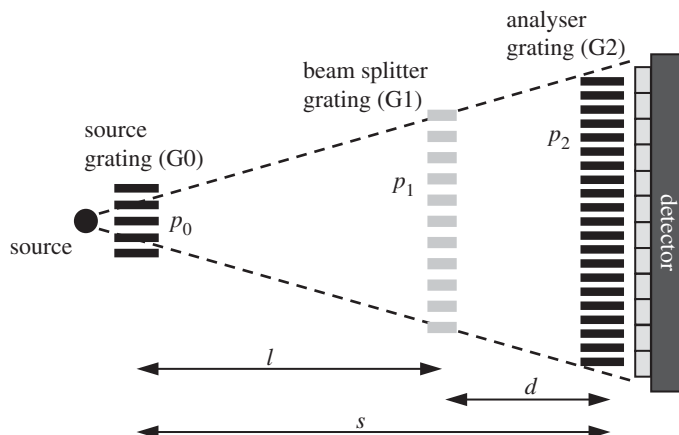


**Figure 1.** System parameters of a grating interferometer. The Talbot-type interferometer consists of two gratings (G1 and G2), whereas the Talbot–Lau-type interferometer uses an additional grating in front of the source (G0).

G1 periodically shifts the phase by  $\pi/2$  and zero, and thus it is referred to as a  $\pi/2$ -shifting phase grating. For  $\eta = 2$ , G1 introduces a periodic phase shift of  $\pi$  and zero and it is called a  $\pi$ -shifting phase grating.

G2 is the analyser grating with periodic absorbing structures of period  $p_2$ , translating slight changes of the interference fringes into intensity changes at the detector [2]. The geometric relation between G1 and G2 is given by

$$p_2 = \frac{p_1}{\eta} \frac{s}{l} = p_{11} \frac{s}{l}, \quad (2.2)$$

where  $p_{11} = p_1/\eta$  is the period of a  $\pi/2$ -shifting G1.

The source grating, or G0, is used if the spatial coherence of the beam is too small for the interference formation [4] (Talbot–Lau configuration). The period of G0 must obey

$$p_0 = \frac{l}{d} p_2. \quad (2.3)$$

## (b) Visibility

In the phase-stepping approach of grating interferometry, the phase-stepping curve  $I_p(x)$  is acquired by moving one of the gratings in the transverse beam direction over a grating period and by recording the pixel intensity at multiple, equidistant steps [14]. Assuming a monochromatic beam and taking into account the finite source size, the continuous (unsampled) phase-stepping curve is given by a convolution of the coherent interference pattern  $I_c(x)$ , the projected source-intensity profile  $S'(x)$  and the transmission function  $G(x)$  of G2 [16],

$$I_p(x) = I_c(x) * S'(x) * G(x). \quad (2.4)$$

At the fractional Talbot distances  $d_m$  (see equation (2.1)), the coherent interference pattern  $I_c(x)$  is given by [16]

$$I_c(x) = 2I_0 T_{0.5,0}(x), \quad (2.5)$$

where the function  $T_{\kappa,\tau}(x)$  is a rectangular pulse train of period  $p_2$ , duty cycle  $\kappa$  and transmission coefficient  $\tau$  (figure 2) and  $I_0$  is the source intensity, specifying the number of emitted photons per second and unit solid angle.

The projected source profile  $S'(x)$  can be either the shape of the focal spot in an X-ray tube (Talbot-type interferometer) or an array source, generated by a source grating (G0 of a Talbot–Lau-type interferometer). As the shape of the source influences the shape of  $I_p(x)$ , the projected

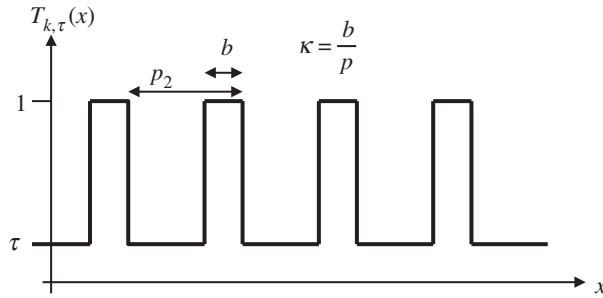


**Figure 2.** Generalized intensity transmission function, used for the coherent interference pattern  $I_c(x)$ , the projected transmission function  $S'_{TL}(x)$  of G0 and the transmission function  $G(x)$  of G2. The function has a constant period  $p_2$  and allows for a custom duty cycle  $\kappa = b/p$  and a non-ideal transmission factor  $\tau \geq 0$ .

source profiles of the Talbot-type and Talbot–Lau-type interferometers are treated separately by using  $S'_T(x)$  (Talbot) and  $S'_{TL}(x)$  (Talbot–Lau) and are expressed as [16]

$$S'_T(x) = \frac{1}{\sigma'_s \sqrt{2\pi}} \exp(-x^2/2\sigma'^2_s) \quad (2.6)$$

and

$$S'_{TL}(x) = T_{\kappa_0, \tau_0}(x). \quad (2.7)$$

The projected source-intensity profile for the Talbot interferometer,  $S'_T(x)$ , is assumed to be a Gaussian with a standard deviation of  $\sigma'_s$ . The true source size  $\sigma_s$  and the projected source size  $\sigma'_s$  are related by

$$\sigma'_s = \sigma_s \frac{d}{l} = \sigma_s \frac{p_2 - p_{11}}{p_{11}}. \quad (2.8)$$

Similarly, the projected period of G0 is given by  $p'_0 = p_0 \cdot d/l = p_2$ , which explains why, in equation (2.7),  $S'_{TL}(x)$  is given by the rectangular pulse train function  $T_{\kappa_0, \tau_0}(x)$  with period  $p_2$ . The duty cycle and the transmission of the grating lines of G0 are given by  $\kappa_0$  and  $\tau_0$ , respectively.

The transmission function of G2 can be expressed as [16]

$$G(x) = T_{\kappa_2, \tau_2}(x), \quad (2.9)$$

which again uses the rectangular pulse train function  $T_{\kappa, \tau}(x)$  displayed in figure 2, with the duty cycle  $\kappa_2$  and the transmission  $\tau_2$ .

The visibility  $V$  is defined as the normalized amplitude of  $I_p(x)$  (equation (2.4)), given by [14]

$$V = \frac{I_{p, \max} - I_{p, \min}}{I_{p, \max} + I_{p, \min}}. \quad (2.10)$$

As  $I_p(x)$  is a periodic function of period  $p_2$ , its Fourier transform,  $\hat{I}_p[n]$ , is a discrete spectrum with non-zeros at the frequencies  $n \cdot 1/p_2$  ( $n \in \mathbb{N}^0$ ). The standard approach for the analysis of the phase-stepping curve uses only the Fourier coefficient at the frequency  $1/p_2$  ( $n = 1$ ), as the higher frequency components are usually low and can be neglected. In this case, the visibility is given by [11]

$$V = 2 \frac{\hat{I}_p[1]}{\hat{I}_p[0]} \quad (2.11)$$

$$= 2 \frac{\hat{I}_c[1] \cdot \hat{S}'[1] \cdot \hat{G}[1]}{\hat{I}_c[0] \cdot \hat{S}'[0] \cdot \hat{G}[0]}. \quad (2.12)$$

In the Fourier domain, equations (2.5)–(2.7) and (2.9) are given by

$$\hat{I}_c[n] = I_0 \operatorname{sinc}\left(\frac{n}{2}\right), \quad (2.13)$$

$$\hat{S}'_T[n] = \exp(-2(n\pi\sigma_s((p_2 - p_{11})/(p_2 \cdot p_{11})))^2), \quad (2.14)$$

$$\hat{S}'_{TL}[n] = \tau_0 \delta[n] + \kappa_0(1 - \tau_0) \operatorname{sinc}(n\kappa_0) \quad (2.15)$$

and

$$\hat{G}[n] = \tau_2 \delta[n] + \kappa_2(1 - \tau_2) \operatorname{sinc}(n\kappa_2), \quad (2.16)$$

where  $\delta[n]$  is the Kronecker delta function and  $\operatorname{sinc}(x) = \sin(\pi x)/\pi x$ . Using these equations, the visibility can be calculated for the Talbot and the Talbot–Lau cases,

$$V = 2 \frac{|\hat{I}_p[1]|}{|\hat{I}_p[0]|} = \frac{4}{\pi} \cdot V_{G2}^* \cdot V_{S'}^*, \quad (2.17)$$

with

$$V_{G2}^* = \frac{\kappa_2(1 - \tau_2) \operatorname{sinc}(\kappa_2)}{\tau_2 + \kappa_2(1 - \tau_2)}, \quad (2.18)$$

$$V_{S,TL}^* = \frac{\kappa_0(1 - \tau_0) \operatorname{sinc}(\kappa_0)}{\tau_0 + \kappa_0(1 - \tau_0)} \quad (2.19)$$

and

$$V_{S,T}^* = \exp(-2(\pi\sigma_s((p_2 - p_{11})/(p_2 \cdot p_{11})))^2). \quad (2.20)$$

For the case where G0 and G2 are ideal absorption gratings ( $\tau = 0$ ) with a duty cycle of  $\kappa = 0.5$ , the visibilities become

$$V_T = 2 \left(\frac{2}{\pi}\right)^2 \exp(-2(\pi\sigma_s((p_2 - p_{11})/(p_2 \cdot p_{11})))^2) \quad (2.21)$$

and

$$V_{TL} = 2 \left(\frac{2}{\pi}\right)^3 = 0.516 = \text{const.} \quad (2.22)$$

These equations are consistent with what has already been reported in the literature [16,17]. It is important to point out here that the visibility of a Talbot interferometer is dependent on the grating pitches, whereas this dependency does not exist for the Talbot–Lau type.

### (c) Smallest detectable refraction angle

The SNR is a widely used metric for the optimization of the system performance. For the differential phase-contrast image [1,2] of a grating interferometer, it can be shown [12] that the SNR is given by

$$\text{SNR}_\varphi = \frac{\varphi}{\sigma_\varphi} = \alpha \underbrace{\frac{2\pi d}{p_2}}_\varphi \underbrace{\frac{V\sqrt{N}}{\sqrt{2\chi_{\text{det}}}}}_{1/\sigma_\varphi}. \quad (2.23)$$

The signal  $\varphi$  corresponds to the lateral displacement of the interference fringes, which occurs if the beam is refracted by an angle  $\alpha$  by the object. The noise standard deviation of the signal, given by  $\sigma_\varphi$ , depends on the number of counts  $N$  on the detector (analogue-to-digital units; ADUs), on the visibility  $V$  and on the detector-specific parameter  $\chi_{\text{det}}$ , which specifies the number of ADUs per incoming photon [18,19]. Other sources of noise such as jitter from mechanical instabilities or aliasing owing to the discrete sampling of the phase-stepping curve are not considered here.

In equation (2.23), signal *and* noise are dependent on the geometric parameters. Separating this equation into a geometry-independent and a geometry-dependent part yields

$$\text{SNR}_\alpha = \frac{\alpha}{\sigma_\alpha} = \alpha \underbrace{\frac{2\pi d}{p_2} \frac{V\sqrt{N}}{\sqrt{2\chi_{\text{det}}}}}_{1/\sigma_\alpha}. \quad (2.24)$$

Essentially, this is the same equation as equation (2.23); however, this equation specifies the signal of the refraction angle  $\alpha$  versus its standard deviation  $\sigma_\alpha$ . The refraction angle  $\alpha$  is geometry independent, and therefore the minimization of  $\sigma_\alpha$  can be used for the optimization of the geometry [11,12]. Here,  $\sigma_\alpha$  is defined as the smallest detectable refraction angle and is given by

$$\alpha_{\min} \equiv \sigma_\alpha = \frac{p_2}{2\pi d} \frac{\sqrt{2\chi_{\text{det}}}}{V\sqrt{N}}. \quad (2.25)$$

In the literature,  $\alpha_{\min}$  has been referred to as the sensitivity [11,12]. As the sensitivity has also been defined differently [10,20], here  $\alpha_{\min}$  is just referred to as the smallest detectable refraction angle.

The proportionality of  $\alpha_{\min}$  to  $p_2/d$  suggests using a small analyser grating pitch and long experimental arrangements, which can be achieved with higher Talbot order designs. However, the counterpart of long arrangements is the inverse quadratic relation with the flux for a given source and detector system. Taking into account both effects requires us to consider the time-dependent  $\alpha_{\min}$  [12]. Using equations (2.2) and (2.3) and the geometric relation  $s = d + l$ , for the Talbot interferometer, the factor  $p_2/d$  becomes

$$\frac{p_2}{d} = \frac{1}{s} \frac{p_2^2}{p_2 - p_{11}}. \quad (2.26)$$

For the Talbot–Lau interferometer, this factor becomes

$$\frac{p_2}{d} = \frac{1}{s} (p_0 + p_2). \quad (2.27)$$

The number of counts  $N$  on the detector can be expressed by [12]

$$N = I_0 D \chi_{\text{det}} \frac{a^2}{s^2} t_{\text{exp}}, \quad (2.28)$$

where  $t_{\text{exp}}$  is the total exposure time (all phase steps) and  $a$  is the pixel size (quadratic pixels) of the detector. The parameter  $D$  accounts for any absorption of the X-rays in the gratings and their substrates and for the detector efficiency. By inserting equations (2.26) and (2.28) into equation (2.25),  $\alpha_{\min}$  for the Talbot and the Talbot–Lau interferometers becomes, respectively,

$$\alpha_{\min, \text{T}} = \frac{1}{2\pi} \frac{p_2^2}{V_{\text{T}}(p_2 - p_{11})} \frac{\sqrt{2}}{a\sqrt{I_0 D t_{\text{exp}}}} \quad (2.29)$$

and

$$\alpha_{\min, \text{TL}} = \frac{1}{2\pi} \frac{p_0 + p_2}{V_{\text{TL}}} \frac{\sqrt{2}}{a\sqrt{I_0 D t_{\text{exp}}}}. \quad (2.30)$$

Equations (2.29) and (2.30) show that, for a given source and detector system,  $\alpha_{\min}$  is independent of the arrangement length  $s$  and the Talbot order  $m$ . For constant grating periods, any increase in  $s$  (and thus  $m$ ), which increases the fringe signal  $\varphi$ , is compensated by the lower photon flux at the detector. This result is, strictly speaking, only valid if the spacings between G2 and the detector as well as between the source and G0 (only in the Talbot–Lau case) are much smaller than  $s$ .

$\alpha_{\min}$  is also independent of the phase-grating parameter  $\eta$ . It will be shown later that this result is only valid for the case of a monochromatic beam.

Essentially,  $\alpha_{\min}$  is mainly dependent on the grating parameters (i.e. the periods and duty cycles). In §3, a complete optimization of the geometry is presented by using equations (2.29) and (2.30) and the analytical expressions of the visibilities, which were derived in §2b (equations (2.17)–(2.20)).

### 3. Optimization of the geometry

For a full optimization of the grating interferometer geometry, a few remaining dependencies must be taken into account. For the Talbot interferometer, the flux  $I_0$  is typically proportional to the output power of the tube or the source size ( $I_0 \propto \sigma_s$ ). The reduction of the flux by the non-ideal transmission of G0 and G2 and by their duty cycles is considered by using  $D \propto \tau + \kappa(1 - \tau)$ . By inserting the expressions for the visibility derived in §2 into equations (2.29) and (2.30),  $\alpha_{\min}$  becomes

$$\alpha_{\min,T} = \frac{\gamma_1(\kappa_2, \tau_2) \cdot \gamma_2(p_{11}, p_2, \sigma_s)}{4a\sqrt{2t_{\text{exp}}}} \quad (3.1)$$

and

$$\alpha_{\min,TL} = \frac{\gamma_1(\kappa_0, \tau_0) \cdot \gamma_1(\kappa_2, \tau_2) \cdot \gamma_3(p_0, p_2)}{4a\sqrt{2I_0 t_{\text{exp}}}}, \quad (3.2)$$

with

$$\gamma_1(\kappa, \tau) = \frac{\sqrt{\tau + \kappa(1 - \tau)}}{\kappa(1 - \tau) \text{sinc}(\kappa)}, \quad (3.3)$$

$$\gamma_2(p_{11}, p_2, \sigma_s) = \frac{p_2^2}{p_2 - p_{11}} \frac{\exp(2(n\pi\sigma_s((p_2 - p_{11})/(p_{11} \cdot p_2)))^2)}{\sqrt{\varrho\sigma_s}} \quad (3.4)$$

and

$$\gamma_3(p_0, p_2) = p_0 + p_2. \quad (3.5)$$

In equation (3.4), the parameter  $\varrho$  is only for the purpose of maintaining correct units. The above equations can be used to optimize all geometric parameters.

In order to find optimum values, the derivatives of  $\gamma_1$ ,  $\gamma_2$  and  $\gamma_3$  can be set to zero. The optimization of  $\gamma_1(\kappa, \tau)$  mainly involves finding the optimum duty cycle for a given transmission factor  $\tau$ . No analytical solution exists for  $\partial\gamma_1/\partial\kappa = 0$ , and thus the function  $\gamma_1(\kappa, \tau)$  (normalized) has been numerically evaluated for different values of  $\tau$  in figure 3a. The optimum values for the duty cycle as a function of  $\tau$  are shown in figure 3b. An interesting result here is that the optimum duty cycle for an ideal absorption grating ( $\tau = 0$ ) is given by  $\kappa = 0.371$ . This value is consistent with a result reported earlier [13].

The derivative of  $\gamma_2(p_{11}, p_2, \sigma_s)$  with respect to  $p_{11}$  can be set to zero to find the optimum  $p_{11}$  (or  $p_1 = \eta p_{11}$ ) as a function of  $p_2$  and  $\sigma_s$ . An analytical solution exists but is not given here owing to its rather complex form. Instead, figure 4a shows  $\gamma_2$  (normalized) for different focal spot sizes of the source,  $w = 2\sqrt{2 \ln 2} \sigma_s$  (full width at half maximum (FWHM)), and for a fixed period  $p_2 = 2.4 \mu\text{m}$  of G2. First, this plot shows that there exists an optimum  $p_1$  (black markers) for a given  $p_2$  and source size  $w$ . This relation is of high practical importance, because  $w$  and  $p_2$  are usually fixed by the available X-ray source and by the smallest achievable absorption grating period. Figure 4b shows the optimum  $p_{11}$  as a function of the source size  $w$ . Second, the plot in figure 4a indicates that, for smaller source sizes  $w$ , smaller grating pitches  $p_1$  can be used, which essentially increases the Talbot order for a fixed  $p_2$ . The simultaneous reduction of  $w$  and  $p_1$  reduces  $\gamma_2$ .

For a Talbot interferometer, the optimum strategy is to select the smallest possible period for G2, such that the grating structures are still high enough for an efficient absorption. The optimum duty cycle  $\kappa_2$  of G2 depends on the transmission factor  $\tau_2$  and can be calculated by using equation (3.3). For ideal absorption properties of G2, the optimum duty cycle is  $\kappa_2 = 0.371$ . The optimum period for G1 can then be calculated by using equation (3.4) for the selected  $p_2$  and



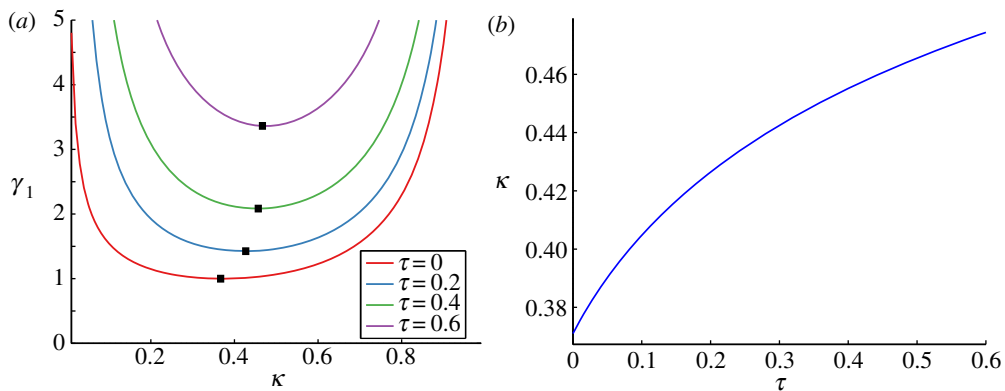


**Figure 3.** Optimization of an absorption grating (G0 or G2). (a) Normalized  $\gamma_1$  as a function of  $\kappa$  for different transmission factors  $\tau$  of the absorption grating. The minima are marked with black spots. (b) Optimum duty cycle  $\kappa$  as a function of  $\tau$  (positions of the black rectangles in (a)). (Online version in colour.)

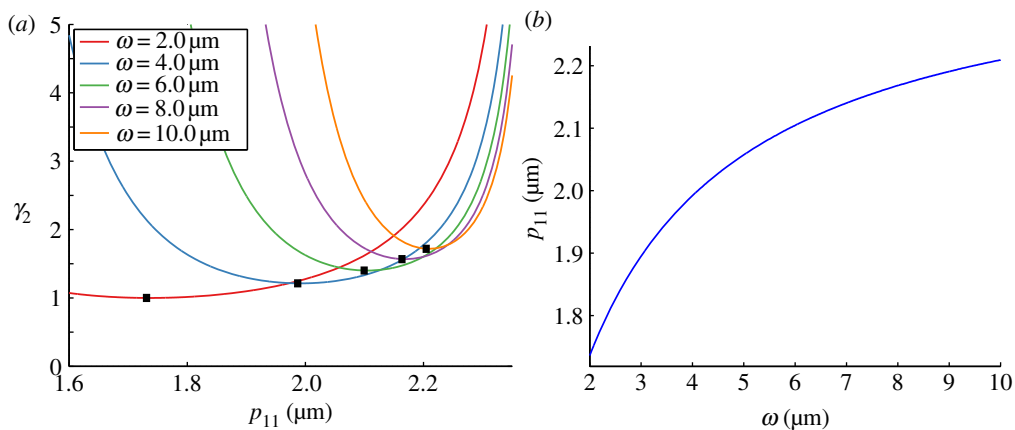


**Figure 4.** Optimization of a Talbot interferometer. (a) Normalized  $\gamma_2$  as a function of  $p_{11} = p_1/\eta$  for different source sizes  $w$  (FWHM) and for  $p_2 = 2.4\ \mu\text{m}$ . The minima are at the black markers. (b) Optimum  $p_{11}$  (from the positions of the black rectangles in (a)) as a function of source size  $w$ . (Online version in colour.)

for a given source size  $w$ . The arrangement length  $s$  is finally determined by  $p_1$ ,  $p_2$  and by the selected Talbot order  $m$  and can be derived by using equations (2.1) and (2.2)

$$s = l + d = \frac{m}{2\lambda_0} \frac{p_1 p_2^2}{\eta p_2 - p_1}, \quad (3.6)$$

where  $\lambda_0$  is the design wavelength.

For the Talbot–Lau interferometer, the optimization of the geometry is simpler. According to equation (3.5),  $\gamma_3$  is minimized for the smallest sum of the grating periods  $p_0$  and  $p_2$ . As both gratings normally have the same requirements for the structure height, the fabrication is, apart from the required area, the same. Therefore, the optimum selection is  $p_0 = p_2$ , yielding a symmetric interferometer arrangement ( $l = d = s/2$  and  $p_0 = p_1 = p_2$ ).

For the selection of the duty cycle of G0, it depends on whether one aims at the optimization of the SNR per time or the SNR per dose. In the former case, the previously described optimum of an absorption grating, or  $\kappa_0 = 0.371$  (for ideal absorption), is valid. In the latter case, the optimization of G0 is theoretically given by  $\kappa_0 \rightarrow 0$ , as, in this case, the visibility is maximized, yielding the maximum efficiency of the used photons to acquire a phase image. Of course,

in practice, this is not a feasible solution, because  $\kappa_0 \rightarrow 0$  leads to  $t_{\text{exp}} \rightarrow \infty$ . Therefore,  $\kappa_0$  would have to be selected such that the visibility is high enough to achieve the required SNR per dose.

## 4. Polychromatic performance

The design energy of the grating interferometer represents the X-ray energy for which the system geometry is optimized. When using a polychromatic beam, X-rays with an energy other than the design energy undergo a different phase shift in G1 and result in an interference pattern with a reduced visibility. In this section, the effect of a polychromatic beam on the performance of the grating interferometer is quantitatively analysed by evaluating the polychromatic fringe visibility, which is the visibility of the interference pattern prior to phase stepping. The fringe visibility is different from the true visibility of the phase stepping curve; however, they are proportional if an ideal G2 ( $\tau_2 = 0$ ) is used. From the polychromatic visibility, the smallest detectable refraction angle with a polychromatic beam can be obtained by using equation (2.24), although this is only valid if there is no object in the beam (flat field) [18,21]. With an object, this is an approximation which neglects the dispersion.

### (a) Energy-dependent fringe visibility

For the calculation of the polychromatic fringe visibility (see §4b), first, a wavelength-dependent analysis of the interference pattern is required. The interference pattern is generated by a convolution of the complex transmission function of G1, given by  $T_1(x)$ , and the Fresnel propagator  $P_z(x)$ . In the Fourier domain, this can be expressed by

$$\hat{\psi}_{z,\lambda}(v) = \hat{T}_{1,\lambda}(v) \cdot \hat{P}_{z,\lambda}(v). \quad (4.1)$$

The Fresnel propagator in the Fourier domain is given by

$$\hat{P}_{z,\lambda}(v) = \exp(-i\pi\lambda z v^2), \quad (4.2)$$

and the transmission function of G1 is defined as

$$T_{1,\lambda}(x) = \exp(i\phi(\lambda)U_1(x)), \quad (4.3)$$

where  $U_1(x)$  is a pulse train function of period  $p_1$ , with a low value of zero and a high value of one. The function  $\phi(\lambda)$  is the phase shift introduced by G1, which is dependent on the material and the grating height. Without proof, the Fourier coefficients of  $T_{1,\lambda}(x)$  are then given by

$$\hat{T}_{1,\lambda}[n] = \begin{cases} \frac{1 + \exp(i\phi(\lambda))}{2} & n = 0 \\ 0 & n \text{ even} \\ \frac{1 - \exp(i\phi(\lambda))}{i\pi n} & n \text{ odd.} \end{cases} \quad (4.4)$$

For a material with a homogeneous refraction index decrement  $\delta$  (which is assumed here for G1), the phase shift introduced to the wave front can be expressed by  $\phi(\lambda) = k\delta(\lambda)h_1 \propto \lambda h_1$ , where  $k = 2\pi/\lambda$  is the wave number,  $h_1$  is the structure height of G1 and the right-hand side has been obtained by using the relationship  $\delta(\lambda) \propto \lambda^2$ . As only the two cases of a  $\pi/2$  and a  $\pi$ -shifting phase grating are considered, the condition  $\phi(\lambda_0) = \lambda_0 h_1 = \eta(\pi/2)$  finally results in

$$\phi(\lambda) = \eta \frac{\pi}{2} \frac{\lambda}{\lambda_0}. \quad (4.5)$$

For the calculation of the fringe visibility, the Fourier transform of the intensity of  $\psi_{z,\lambda}(x)$  is required

$$I_{z,\lambda}(x) = |\psi_{z,\lambda}(x)|^2 = \psi_{z,\lambda}(x) \cdot \psi_{z,\lambda}^*(x) \quad (4.6)$$

and

$$\hat{I}_{z,\lambda}[n] = \hat{\psi}_{z,\lambda}[n] * \hat{\psi}_{z,\lambda}^*[n]. \quad (4.7)$$

As  $I_{z,\lambda}(x)$  is a periodic function, it has a discrete Fourier spectrum, expressed by  $\hat{I}_{z,\lambda}[n]$ . Equation (4.7) essentially shows that a discrete convolution is necessary to obtain the Fourier coefficients of the intensity pattern. As we are only interested in the zeroth, first and second Fourier coefficients, the convolution can be computed for those points. Without proof, the Fourier coefficients at the odd fractional Talbot order distances ( $m \in \{1, 3, 5, \dots\}$ ) are given by

$$\hat{I}_\lambda[0] = 1, \quad (4.8a)$$

$$\hat{I}_\lambda[1] = \frac{2}{\pi} i \sin\left(\frac{\pi}{2} \eta \frac{\lambda}{\lambda_0}\right) \sin\left(\frac{\pi}{2} \frac{m}{\eta^2} \frac{\lambda}{\lambda_0}\right) \quad (4.8b)$$

$$\text{and} \quad \hat{I}_\lambda[2] = -\frac{2}{\pi} \sin^2\left(\frac{\pi}{4} \eta \frac{\lambda}{\lambda_0}\right) \left| \sin\left(2\pi \frac{m}{\eta^2} \frac{\lambda}{\lambda_0}\right) \right|. \quad (4.8c)$$

The second Fourier coefficient is required for the case  $\eta = 2$ , as, in that case, the fringe period is compressed by a factor of 2. The wavelength-dependent normalized fringe visibility is then given by

$$\begin{aligned} v_\lambda &= \frac{|\hat{I}_\lambda[\eta]|}{|\hat{I}_\lambda[0]|} \\ &= \frac{2}{\pi} \left| \sin^\eta\left(\pi \frac{\lambda}{2\lambda_0}\right) \sin\left(m\pi \frac{\lambda}{2\lambda_0}\right) \right|. \end{aligned} \quad (4.9)$$

Equation (4.9) provides a deep insight into the energy-dependent behaviour of the grating interferometer. For instance, the zero crossings of  $v(\lambda)$ , which are located at

$$\lambda_{v=0} = 2 \frac{n}{m} \lambda_0, \quad n \in \mathbb{N}, \quad (4.10)$$

can be used to study the spectral acceptance. If the spectral acceptance is defined as the spectral width between the two zero crossings around the design wavelength  $\lambda_0$  or around the design energy  $E_0$ , respectively, it can be expressed by

$$\Delta\lambda = 2 \frac{\lambda_0}{m} \quad (4.11)$$

and

$$\Delta E \approx 2 \frac{E_0}{m}. \quad (4.12)$$

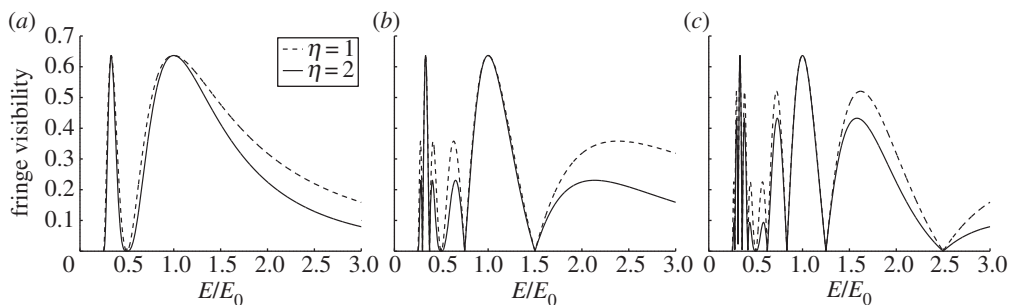
The relative spectral acceptance  $\Delta E/E_0$  is above 10% for Talbot orders below 20, which indicates that the grating interferometer is highly achromatic. This result is consistent with a result reported earlier, where a sinusoidal proportionality of the interference fringe contrast has been used to calculate the half-width between two zero crossings [14].

Figure 5 shows the fringe visibility as a function of the relative energy  $E/E_0$  and at the first, third and fifth fractional Talbot order for  $\eta = 1$  and  $\eta = 2$ . The reduction of the spectral acceptance at higher Talbot orders is clearly visible, which confirms the result from equation (4.12). On the other hand, side lobes of the fringe visibility, appearing at higher and lower energies, will also contribute to the signal when using polychromatic radiation. In §4b, it is demonstrated how the energy-dependent fringe visibility, including the side lobes, affects the polychromatic fringe visibility of the grating interferometer.

## (b) Polychromatic fringe visibility

The polychromatic fringe visibility can be derived from the polychromatic intensity pattern and its Fourier coefficients, which are given by [15,22]

$$I_{\text{poly}}(x) = \int \omega(E) I_E(x) dE \quad (4.13)$$



**Figure 5.** Fringe visibility  $v$  (equation (4.9)) as a function of normalized energy  $E/E_0$  for  $\eta = 1$  (dashed lines) and  $\eta = 2$  (solid lines) for (a)  $m = 1$ , (b)  $m = 3$  and (c)  $m = 5$ . The reduction of the spectral acceptance with increasing Talbot order  $m$  is clearly visible.

and

$$\hat{I}_{\text{poly}}[n] = \int \omega(E) \hat{I}_E[n] dE. \quad (4.14)$$

The first factor in the integrand,  $\omega(E)$ , represents the normalized continuous X-ray spectrum with  $\int \omega(E) dE = 1$ . The energy-dependent intensity pattern is given by  $I_E(x) = I_\lambda(x)$  for  $\lambda = hc/E$  (where  $h$  is the Planck constant and  $c$  is the speed of light). From the Fourier coefficients, the polychromatic fringe visibility can be calculated as

$$\begin{aligned} v_{\text{poly}} &= \frac{|\hat{I}_{\text{poly}}[\eta]|}{|\hat{I}_{\text{poly}}[0]|} \\ &= \frac{|\int \omega(E) \hat{I}_E[\eta] dE|}{|\int \omega(E) \hat{I}_E[0] dE|} \\ &= \left| \int \omega(E) \hat{I}_E[\eta] dE \right|. \end{aligned} \quad (4.15)$$

As the first approximation, the spectrum can be assumed to be a rectangular function with finite support from  $E_0 - \Delta E/2$  to  $E_0 + \Delta E/2$  and height  $1/\Delta E$ . In this case, the polychromatic fringe visibility can be expressed by

$$v_{\text{poly}} = \frac{1}{\Delta E} \int_{E_0 - \Delta E/2}^{E_0 + \Delta E/2} \hat{I}_E[\eta] dE = \bar{\hat{I}}_E[\eta], \quad (4.16)$$

where  $\bar{\hat{I}}_E[\eta]$  is the mean of  $\hat{I}_E[\eta]$  in the interval from  $E_0 - \Delta E/2$  to  $E_0 + \Delta E/2$ .

A more realistic selection for the shape of the spectrum is a Gaussian; however, no analytical solution can then be obtained for the polychromatic fringe visibility. Figure 6a shows a plot of the polychromatic fringe visibility as a function of the relative bandwidth  $\Delta E/E_0$  (FWHM) of a Gaussian spectrum for different Talbot orders and for  $\eta = 1$  (dashed lines) and  $\eta = 2$  (solid lines). In each case, the maximum fringe visibility at  $\Delta E/E_0 = 0$  amounts to  $2/\pi = 0.637$ , which corresponds to the fringe visibility when using a monochromatic beam from a point source. For  $\Delta E/E_0 > 0$ , the reduction of the fringe visibility is clearly visible. A significant difference can be observed between the polychromatic performance of  $\pi$  and  $\pi/2$ -shifting phase gratings (parameter  $\eta$ ), which is discussed in more detail in §4c.

### (c) Type of beam splitter grating

The previous results can be used to investigate the properties of a  $\pi$  versus a  $\pi/2$ -shifting phase grating. Using the approximation that the polychromatic fringe visibility is given by

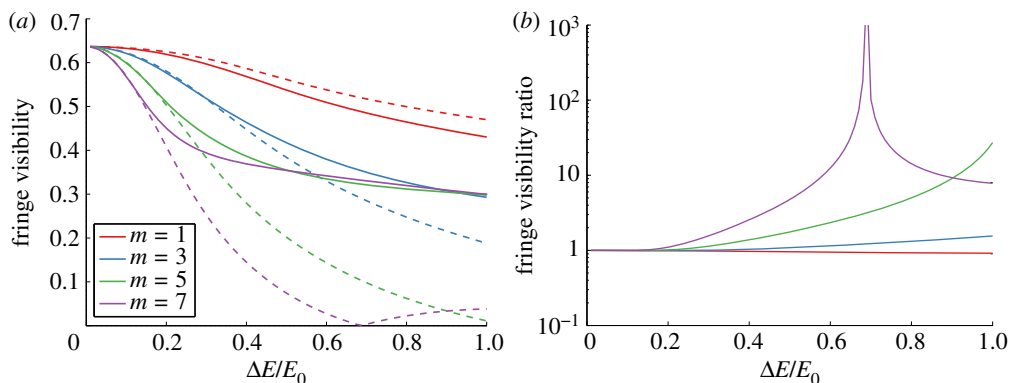


**Figure 6.** (a) Fringe visibility for a polychromatic beam of a point source as a function of the normalized energy bandwidth  $\Delta E/E_0$  of a Gaussian spectrum (FWHM) for  $m \in \{1, 3, 5, 7\}$  and for  $\eta = 1$  (dashed lines) and  $\eta = 2$  (solid lines). (b) Ratio of the fringe visibilities for  $\eta = 2$  versus  $\eta = 1$ . A  $\pi$ -shifting phase grating generally shows a higher polychromatic fringe visibility, except for the case of the first fractional Talbot order ( $m = 1$ ). (Online version in colour.)

equation (4.16), the mean value of  $\hat{I}_E[\eta]$  evolves completely differently for  $\eta = 1$  compared with  $\eta = 2$  when increasing the bandwidth  $\Delta E$ .

For  $\eta = 1$ ,  $\hat{I}_E[1]$  can change the sign after a zero crossing in the spectral domain (see equation (4.8b)), leading to negative values which can cause a rapid decay of the mean value of  $\hat{I}_E[1]$ , and thus of  $v_{\text{poly}}$ . In the spatial domain, negative values of  $\hat{I}_E[1]$  are equivalent to a shift of the interference pattern by  $\pi$ , causing a fringe contrast inversion. This effect negatively affects the polychromatic performance of the grating interferometer. In figure 6a, which shows  $v_{\text{poly}}$  for a Gaussian spectrum, the rapid decay for  $\eta = 1$  is clearly visible (dashed lines). An exception occurs at the first fractional Talbot order ( $m = 1$ ), where  $\hat{I}_E[1]$  is always positive (no fringe contrast inversion), resulting in a slow decay of  $v_{\text{poly}, \eta=1}$ .

For  $\eta = 2$ , no fringe contrast inversion occurs, because  $\hat{I}_E[2]$  cannot be negative in the spectral domain (see equation (4.8c)). Therefore, the decay of  $v_{\text{poly}, \eta=2}$  is much slower than that of  $v_{\text{poly}, \eta=1}$ . On the other hand, as one of the sines in  $\hat{I}_E[2]$  is squared,  $v_{\text{poly}, \eta=2}$  initially decays slightly faster than  $v_{\text{poly}, \eta=1}$ . Owing to this effect,  $v_{\text{poly}, \eta=1}$  is slightly higher than  $v_{\text{poly}, \eta=2}$  at the first fractional Talbot order. However, with a maximum gain of approximately 8.5% at a relative bandwidth of  $\Delta E/E = 1$ , this effect is relatively weak. At higher Talbot orders ( $m > 1$ ), it is negligible (maximum gain is less than 1%).

Figure 6b shows the ratio of the polychromatic fringe visibilities for a  $\pi$ -shifting versus a  $\pi/2$ -shifting phase grating. The plot shows that a  $\pi/2$  grating slightly outperforms a  $\pi$  grating at the first fractional Talbot order, however the gain is marginal (4.3% at  $\Delta E/E = 0.5$ ). At higher Talbot orders ( $m > 1$ ), it is recommended to use a  $\pi$  grating. At  $\Delta E/E = 0.5$ , the gain is 8.8% for  $m = 3$ , 75.8% for  $m = 5$  and 477% for  $m = 7$ .

## 5. Summary and discussion

The smallest detectable refraction angle  $\alpha_{\min}$  for the Talbot-type and the Talbot–Lau-type interferometers has been analysed. The dependency of  $\alpha_{\min}$  on the source and detector system (focal spot size, beam intensity, pixel size and detection efficiency) and the parameters of the grating interferometer (periods, duty cycles, beam splitter grating type and non-ideal absorption) have been derived analytically with the aim of optimizing the interferometer geometry. For the Talbot interferometer,  $\alpha_{\min}$  is minimized for smallest source sizes  $w$  and smallest analyser grating periods  $p_2$ . The minimization of  $p_2$  is limited by the grating fabrication technology. For a given  $p_2$  and  $w$ , an optimum for  $p_1$  can be calculated by using the methods presented here. The fabrication of the appropriate G1 is usually not a limiting factor.

For the Talbot–Lau interferometer,  $\alpha_{\min}$  is minimized for the smallest sum of  $p_0$  and  $p_2$ , which means that the limitation is also given by the grating technology.

For both interferometer types, the optimum duty cycle for G2 depends on its transmission factor  $\tau_2$ . For  $\tau_2 = 0$ , the duty cycle should be  $\kappa_2 = 0.371$ . The source grating of a Talbot–Lau interferometer has the same optimum,  $\kappa_0 = 0.371$ , if the aim is to maximize the SNR per time. For an optimization of the SNR per dose,  $\kappa_0$  has to be chosen to yield the required visibility.

The polychromatic performance of the grating interferometer was studied quantitatively by analytically deriving the relationship between interference fringe visibility and photon energy. The spectral acceptance, which is the width of the spectrum between the two zero crossings of the fringe visibility around the design energy, is an indicator of the polychromatic performance. However, side lobes of the fringe visibility showed that the photons with energies outside the spectral acceptance also contribute to the signal and have to be taken into account for a polychromatic beam. For a  $\pi/2$ -shift grating, a fringe contrast inversion occurs at wavelengths outside of the spectral acceptance and for  $m > 1$ , which leads to a rapid decay of the polychromatic fringe visibility at higher bandwidths. In general, a  $\pi$ -shift phase grating is more favourable for X-ray beams with a broad bandwidth, except for the first fractional Talbot order ( $m = 1$ ), where a  $\pi/2$ -shift grating slightly outperforms the  $\pi$ -shift grating.

As  $\alpha_{\min}$  is, at least for the monochromatic case, independent of the Talbot order for a given source and detector system and for fixed grating periods, the selection of the arrangement length (or the Talbot order) mainly depends on the application. In general, it is always recommended to operate at low Talbot orders, as in this case the spectral acceptance is maximum. Short arrangements (less than 1 m) are favourable for high-resolution applications, where a microfocus source is necessary. The arrangement must be short owing to the low flux of such a tube. Both types—that is, the Talbot-type and Talbot–Lau-type interferometers—are feasible for such a compact arrangement [23]. Two main drawbacks of a compact arrangement are the high divergence of the beam and the typically small space for samples. The former can be solved by using curved gratings [24]. The latter represents a problem owing to the object position-dependent sensitivity [20,25], where  $\alpha_{\min}$  is proportional to the distance from the object to G1. In the extreme case, where the distance between the source and G1 is comparable to the sample size, the position-dependent  $\alpha_{\min}$  in the sample ranges from  $\sigma_{\alpha} = \infty$  (at source) to  $\sigma_{\alpha,\min}$  (at G1). This problem vanishes for longer arrangements, when the sample size is much smaller than the distance between G0 and G1. A long arrangement (more than 1 m) normally requires a source with high output power and consequently with a larger focal spot, and thus only Talbot–Lau configurations are feasible. Long arrangements with a high-power source usually have a smaller  $\alpha_{\min}$  than compact arrangements with a microfocus source, because the output power of the source (and thus the beam intensity  $I_0$ ) is typically increased by around three orders of magnitude (i.e. from W to kW), whereas the square of the distance increases by maximally two orders (i.e. from  $\text{cm}^2$  to  $\text{m}^2$ ).

Achieving high sensitivity with grating interferometer-based phase-contrast imaging on X-ray tubes is still challenging, the technique does not yet allow the higher interaction cross section of the phase compared with absorption to be fully exploited. The challenge is partly given by the critical spatial and temporal coherence (i.e. by the source size and the bandwidth), but also by the currently available grating technology. The development towards smaller grating periods, higher absorption efficiencies and lower attenuation in grating substrates will be crucial to increase the SNR and the gain in CNR compared with absorption imaging.

## References

1. David C, Nöhammer B, Solak H, Ziegler E. 2002 Differential X-ray phase contrast imaging using a shearing interferometer. *Appl. Phys. Lett.* **81**, 3287–3289. (doi:10.1063/1.1516611)
2. Momose A, Kawamoto S, Koyama I, Hamaishi Y, Takai K, Suzuki Y. 2003 Demonstration of X-ray Talbot interferometry. *Jpn J. Appl. Phys.* **42**, L866–L868. (doi:10.1143/JJAP.42.L866)



3. Pfeiffer F, Bech M, Bunk O, Kraft P, Eikenberry E, Brönnimann C, Grünzweig C, David C. 2008 Hard-X-ray dark-field imaging using a grating interferometer. *Nat. Mater.* **7**, 134–137. (doi:10.1038/nmat2096)
4. Pfeiffer F, Weitkamp T, Bunk O, David C. 2006 Phase retrieval and differential phase-contrast imaging with low-brilliance X-ray sources. *Nat. Phys.* **2**, 258–261. (doi:10.1038/nphys265)
5. Pfeiffer F, Bunk O, David C, Bech M, Le Duc G, Bravin A, Cloetens P. 2007 High-resolution brain tumor visualization using three-dimensional X-ray phase contrast tomography. *Phys. Med. Biol.* **52**, 6923–6930. (doi:10.1088/0031-9155/52/23/010)
6. Stampanoni M *et al.* 2011 The first analysis and clinical evaluation of native breast tissue using differential phase-contrast mammography. *Invest. Radiol.* **46**, 801–806. (doi:10.1097/RLI.0b013e31822a585f)
7. Thüring T, Guggenberger R, Alkadhi H, Hodler J, Vich M, Wang Z, David C, Stampanoni M. 2013 Human hand radiography using X-ray differential phase contrast combined with dark-field imaging. *Skelet. Radiol.* **42**, 827–835. (doi:10.1007/s00256-013-1606-7)
8. Raupach R, Flohr T. 2011 Analytical evaluation of the signal and noise propagation in X-ray differential phase-contrast computed tomography. *Phys. Med. Biol.* **56**, 2219–2244. (doi:10.1088/0031-9155/56/7/020)
9. Raupach R, Flohr T. 2012 Performance evaluation of X-ray differential phase contrast computed tomography (PCT) with respect to medical imaging. *Med. Phys.* **39**, 4761–4774. (doi:10.1118/1.4736529)
10. Weitkamp T, Zanette I, Pfeiffer F, David C. 2012 Design aspects of X-ray grating interferometry. *AIP Conf. Proc.* **1466**, 84–89. (doi:10.1063/1.4742273)
11. Modregger P, Pinzer B, Thüring T, Rutishauser S, David C, Stampanoni M. 2011 Sensitivity of X-ray grating interferometry. *Opt. Expr.* **19**, 18 324–18 338. (doi:10.1364/OE.19.018324)
12. Thüring T, Modregger P, Hämmerle S, Weiss S, Nüesch J, Stampanoni M. 2012 Sensitivity in x-ray grating interferometry on compact systems. *AIP Conf. Proc.* **1466**, 293–298. (doi:10.1063/1.4742307)
13. Yashiro W, Takeda Y, Momose A. 2008 Efficiency of capturing a phase image using cone-beam X-ray Talbot interferometry. *J. Optic. Soc. Am. A* **25**, 2025–2039. (doi:10.1364/JOSAA.25.002025)
14. Weitkamp T, Diaz A, David C, Pfeiffer F, Stampanoni M, Cloetens P, Ziegler E. 2005 X-ray phase imaging with a grating interferometer. *Opt. Expr.* **13**, 6296–6304. (doi:10.1364/OPEX.13.006296)
15. Engelhardt M, Kottler C, Bunk O, David C, Schroer C, Baumann J, Schuster M, Pfeiffer F. 2008 The fractional Talbot effect in differential X-ray phase-contrast imaging for extended and polychromatic X-ray sources. *J. Microsc.* **232**, 145–157. (doi:10.1111/j.1365-2818.2008.02072.x)
16. Weitkamp T, David C, Kottler C, Bunk O, Pfeiffer F. 2006 Tomography with grating interferometers at low-brilliance sources. In *Proc. Developments in X-Ray Tomography V, San Diego, CA, 13 August 2006*. Proceedings of SPIE, vol. 6318, pp. 6318–6328. Bellingham, WA: SPIE. (doi:10.1117/12.683851)
17. Diemoz P, Bravin A, Langer M, Coan P. 2012 Analytical and experimental determination of signal-to-noise ratio and figure of merit in three phase-contrast imaging techniques. *Opt. Expr.* **20**, 27 670–27 690. (doi:10.1364/OE.20.027670)
18. Revol V, Kottler C, Kaufmann R, Straumann U, Urban C. 2010 Noise analysis of grating-based X-ray differential phase contrast imaging. *Rev. Sci. Instrum.* **81**, 073709. (doi:10.1063/1.3465334)
19. Engel K, Geller D, Köhler T, Martens G, Schusser S, Vogtmeier G, Rössl E. 2010 Contrast-to-noise in X-ray differential phase contrast imaging. *Nucl. Instrum. Methods Phys. Res. A* **648**, 202–207. (doi:10.1016/j.nima.2010.11.169)
20. Donath T *et al.* 2009 Inverse geometry for grating-based X-ray phase-contrast imaging. *J. Appl. Phys.* **106**, 054703–054703-7. (doi:10.1063/1.3208052)
21. Weber T, Bartl P, Bayer F, Durst J, Haas W, Michel T, Ritter A, Anton G. 2011 Noise in X-ray grating-based phase-contrast imaging. *Med. Phys.* **38**, 4133–4140. (doi:10.1118/1.3592935)
22. Beutel J, Kundel H, Metter RV. 2000 *Handbook of medical imaging: physics and psychophysics*, 2nd edn. Bellingham, WA: SPIE Press.

23. Thüring T, Hämmerle S, Weiss S, Nüesch J, Meiser J, Mohr J, David C, Stampanoni M. 2013 Compact hard X-ray grating interferometry for table top phase contrast micro CT. In *Proc. Medical Imaging 2013: Physics of Medical Imaging, Lake Buena Vista, FL, 9 February 2013*. Proceedings of SPIE, vol. 8668, p. 866813. Bellingham, WA: SPIE. (doi:10.1117/12.2006865)
24. Thüring T, Modregger P, Pinzer B, Wang Z, Rutishauser S, David C, Grund T, Kenntner J, Stampanoni M. 2011 Towards X-ray differential phase contrast imaging on a compact setup. In *Proc. Medical Imaging 2011: Physics of Medical Imaging, Lake Buena Vista, FL, 12 February 2011*. Proceedings of SPIE, vol. 7961, p. 79611G. Bellingham, WA: SPIE.
25. Engelhardt M, Baumann J, Schuster M, Kottler C, Pfeiffer F, Bunk O, David C. 2007 High-resolution differential phase contrast imaging using a magnifying projection geometry with a microfocus X-ray source. *Appl. Phys. Lett.* **90**, 224101. (doi:10.1063/1.2743928)